Progress in Physics of Applied Materials 5 (2025), Serial Number 9, 153– 164

Semnan University

Progress in Physics of Applied Materials

journal homepage: https://ppam.semnan.ac.ir/

Investigation of Thermoelectric Properties of Chalcogenide Semiconductors, $MgBS_3$(B = Hf, Zr): First Principle Approach

Rilwan O Balogun [a*]

[a] *School of Science and Technology, Pan-Atlantic University, Km 52 Lekki-Epe Expressway, Eleko, Ibeju-Lekki, Lagos-state, Nigeria*

ARTICLE INFO

Article history:
Received: 11 February 2025
Revised: 22 March 2024
Accepted: 24 March 2024
Published online: 20 Jun 2025

Keywords:
Crystals of Chalcogenides;
Density Functional Theory;
Seebeck Coefficient;
Thermoelectric Characteristics.

ABSTRACT

Chalcogenide crystals are used in many different industries, but most notably as energy-conversion thermoelectric materials. We have calculated the Seebeck coefficient, electrical conductivity, electronic thermal conductivity, power factor, and figure of merit of $MgBS_3$ (B = Hf, Zr) chalcogenide crystals using semiclassical Boltzmann theory and first-principles calculations. A Quantum Espresso program is used to determine the Fermi level and compute the electronic properties. The transport properties are then computed using the BoltzTraP algorithm. We first make our materials available to the public. We report on our first principle investigation of $MgBS_3$ (B = Hf, Zr), a new class of ternary semiconductor alloys. The structural and elastic properties of these constituents demonstrate their low energy of formation and mechanical stability. In the valence band maximum, the observed electronic energy band gap data show a direct electronic transition including Hf-d states (B = Hf & Zr) along the Γ-symmetry direction, as well as mixed contributions from Mg-s states, Hf-d states, and Zr-d states. Furthermore, to assess the thermoelectric potential of pure $MgHfS_3$ and $MgZrS_3$, the temperature-dependent transport properties were examined. Among the simple measures employed were the "maximum" thermoelectric figure of merit, zT, power factor, Seebeck effect, and their anticipated thermal and electrical conductivity. It provided findings with improved zT values, higher PF, moderate Seebeck effect, and efficient thermal and electrical conductivity compared to the current state of bulk thermoelectric materials. Furthermore, we discover that it is highly improbable to get the necessary zT values for typical device applications by using several additional semiconductors, or chalcogenides perovskites, as described in our work. These results provide an excellent bulk chalcogenide database that is necessary for many potential applications in the renewable energy sector.

1. Introduction

A dimensionless figure of merit of $zT = \frac{TGS^2}{(\kappa_e+\kappa_{ph})}$, where T is the temperature, G is the electronic conductance, S is the Seebeck coefficient, K_e is the electronic thermal conductance, and K_{ph} is the lattice thermal conductance, can be used to quantify the efficiency of a thermoelectric device that directly converts heat and electricity to each other [1-3]. Since thermoelectric devices require low thermal conductance, a big Seebeck coefficient, and a large electronic conductivity, zT ≥ 2 is preferred. Improving the figure of merit is difficult, though, because of the high interaction between these characteristics. It is encouraging that a lot of ideas for enhancing zT have surfaced because of recent work, and several approaches have been put out to address this issue, including creative transport engineering, all scale hierarchical architecture engineering, band structure engineering, and innovative transport engineering.

High-doped semiconductors and unit cells with high average coordination numbers and lots of atoms have attracted a lot of interest [4, 5]. Clathrates [6, 7], skutterudites [8, 9], disordered compounds with high atomic number elements [10], and materials with intrinsically low lattice thermal conductivity, such as

* Corresponding author. Tel.: +234-8154015168
E-mail address: rbalogun@pau.edu.ng, roluwanifemi@yahoo.com

Cite this article as:
Balogun R.O., 2025. Investigation of Thermoelectric Properties of Chalcogenide Semiconductors, $MgBS_3$(B = Hf, Zr): First Principle Approach. *Progress in Physics of Applied Materials*, *5*(2), pp.153-164. DOI: **10.22075/PPAM.2025.36867.1132**

$AgSbTe_2$ [11], are examples of such thermoelectric materials. A single crystal chalcogenide semiconductor called Cu_3SbSe_3 was recently identified by researchers as a new possible TE material after an experiment revealed an unusually low thermal conductivity of 0.7–1.0 W/mK [12]. The extremely low measured thermal conductivity, which is similar to other chalcogenide crystals [13] and well-known thermoelectric materials, has also been attributed to its complex crystal structure because it reduces the effective acoustic mode Debye temperature to low values [14]. But in the last few years, the need to cut back on fossil fuels and environmental concerns have made the creation of new renewable energy sources and materials to replace them essential [15].

Graphene, as an organic material, has relatively weak spin-orbit interaction and weak hyperfine interaction, so that spin memory can be as long as a few seconds [16]. Experimental data have clearly demonstrated that organic molecules can be used as spacers for electronic transport [17]. Spin polarized transport through magnetic molecular layers sandwiched between non-magnetic layers has been demonstrated for systems involving carbon nanotubes [18], other organic π-conjugated systems [19], molecular bridges, and self-assembled organic monolayers [20]. Graphene is a perfect material for spin-polarized electron injection and transport applications in molecular junctions because of these characteristics. Moreover, there has been theoretical research on spin-polarized transport across organic molecules positioned between two contacts [21]. Researchers have investigated the thermal transport through the junctions in addition to the charge transport [22]. The coupling of charge and heat currents in electric conductors produces thermoelectric effects. The conduction and valence bands intersect at the Dirac points, which are situated at the corners of the hexagonal first Brillouin zone, due to graphene's distinct lattice structure [23]. The two-dimensional Dirac-Fermi effect [24], the quantum tunnelling effect, the quantum Hall effect at ambient temperature [25], and many other unique features are caused by the band structure's linear dispersion relation close to the Dirac points. Bipolar nanoelectronics systems may benefit from the use of graphene, a two-dimensional material with several remarkable properties [26].

Low-dimensional or nanoscale systems can exhibit significantly higher zT values than bulk materials, as shown by theoretical predictions and experimental results [27]. For thermoelectric applications, this characteristic may lead to a promising future [28].

Furthermore, the presence of quantum antidots in different materials causes the scattering of electron and phonon-defect. As a result, there is a considerable drop in thermal conductance [29]. Recent experimental studies have focused on quantum antidot arrays. Numerous methods have been used to create these arrays with varying geometries. Novel uses of band structure engineering, lattice anharmonicity, nanowires, nano-structured materials, and two-dimensional materials technology have all been sought to enhance the increasing value of zT [30].

Quantum antidot lattices in graphene have garnered a lot of interest lately. This interest stems from the fact that a band gap, which is necessary for employing graphene in transistor topologies, can be created by creating a variety of holes (quantum antidots) in the graphene layer. The number of separated atoms, the size of the antidot shape, and the geometry of the quantum antidot shape can all be changed to modify the gap's size [31]. Additionally, the thermoelectric characteristics of two-dimensional graphene antidot lattices have been investigated in recent research. As a result, materials with high zT have been produced. Additionally, the ternary chalcogenides, commonly referred to as semiconductors, I–III–VI, and their alloys have been thoroughly discussed in earlier research [32, 33]. These studies show that the materials have notable optoelectronic and thermoelectric properties, which make them promising choices for optoelectronic and photovoltaic applications. This enthusiasm swiftly spread to further family-related resources [34]. Even if there are numerous studies on the compounds in the literature, in-depth research that reveals the compound's fundamental and technological features is still lacking. To create energy materials for future technology, we therefore offer a thorough first principle analysis in this study that highlights the technological aspect of their physical characteristics. In this study, we focus on comparing the physical characteristics of these materials to determine which of these novel ternary semiconductors is best suited for thermoelectric or photovoltaic applications [35].

The electronic transport parameters of the recently proposed material, $MgBS_3$ (B = Hf and Zr) perovskite, were estimated in this study to provide insight into its thermoelectric characteristics. Comparisons between the obtained results and the other well-known TE compounds, $BaZrS_3$-β and $BaZrS_3$-α [35], Na_6ZnX_4 (X=O, S, Se) [36, 37], and $CaInSe_2$ [38], were done to precisely evaluate their bulk thermoelectricity and performance. Along with electronic transport, vibrational characteristics were also calculated to estimate the source of the experimentally observed low lattice thermal conductivity.

2. Computational Approach and Methods

The exchange correlation functional was modeled using the generalized gradient approximation (GGA) in the form of Perdew-Burke-Ernzerhof for solids (PBEsol) [39], and we employed first-principles computations using the Quantum Espresso technique [40]. We have investigated the use of GGA-PBEsol instead of HSE05 since it is suitable for high-throughput material screening of our electron-ion interaction and is more computationally efficient than HSE05. It can also be applied to bigger systems. Additionally, GGA-PBE was used to produce accurate results for our materials based on the use of Hf and Zr elements in the d and f-orbitals. Even though HSE05 usually offers more precise band gaps. The latter was insufficient for our vast material system and was computationally pricey. Moreover, the PBE functional, a specific application of the GGA technique, has been shown to provide acceptable band gaps for a range of materials, including ours, and GGA-PBE thrives in bulk computations where overall structural characteristics are more important than precise band gap values and in studies of materials interacting within metal surfaces. Atoms with valence electrons in Hf, Zr, and S. of [Kr] $4d^2$ $5s^2$, [Ar] $3d^2$ $4s^2$, [Ne]

$3s^2\ 3p^4$, [Xe] $4f^1\ 5d^2\ 6s^2$, and so on were subjected to the all-electron projector augmented wave (PAW) technique. A plane wave set with an energy cut-off of 50 Ry was used to increase the plane waves of the electronic wave functions [41]. The convergence test was conducted with a kinetic energy cut-off of 250 Ry for the charge density and 50 Ry for the plane-wave basis set expansion. The compound's relaxation produced a set of new values for the atomic locations and cell dimensions for the perovskite compounds $MgHfS_3$ and $MgZrS_3$. Denser k-mesh of 12 × 12 × 12 was utilized for density of state and thermoelectric calculations, while a 4 × 4 × 4 k-point mesh sampling technique of Monkhorst-pack was used to simulate the Brillouin Zone integration. The plane-wave basis cutoff was set at 150 Ry to maintain balance between accuracy and velocity. An ultrasoft pseudo-potential was proposed to explain the ionic cores and the valence electron interactions [42]. The Methfessel-Paxton [43] smearing with a Gaussian spreading C = 0.01 Ry was used to expand the energy levels to improve the convergence of the solution of the self-consistent Kohn-Sham equations. A well-converged ground state energy was obtained by setting the total energy convergence in the iterative solution of the Kohn-Sham equations [44] at 1.0×10^{-7} Ry. The BFGS algorithm [45] was used to fully relax all structures with a threshold force of 10^{-3} Ry/Bohr. The Boltzmann transport equations were solved inside the rigid band by the BOLTZTRAP program, and transport calculations were performed using the constant relaxation time (s) approximations. A wide range of thermoelectric materials are compatible with this approach. To guarantee convergence and obtain accurate carrier group velocities—which are essential for determining the transport parameters—the transport calculations were carried out using a 12 × 12 x 12 Monckhorst-Pack k-point grid. The ability to compute TE transport parameters using the semiclassical Boltzmann theory within the BoltzTraP code's constant scattering time approximation (CSTA) is a unique feature of QE [46]. The following equations [47, 48] can be used to express the Seebeck coefficient, electrical conductivity, and electronic thermal conductivity in this theory:

$$S_{\alpha\beta}(T,\mu) = \frac{1}{eT\Omega\sigma_{\alpha\beta}(T,\mu)} \int \sigma_{\alpha\beta}(\varepsilon)(-\mu)\left[-\frac{\delta f_0(T,\varepsilon,\mu)}{\delta\varepsilon}\right] d\varepsilon \quad (1)$$

$$\sigma_{\alpha\beta}(T,\mu) = \frac{1}{\Omega} \int \sigma_{\alpha\beta}(\varepsilon)\left[-\frac{\delta f_0(T,\varepsilon,\mu)}{\delta\varepsilon}\right] d\varepsilon \quad (2)$$

$$\kappa_{\alpha\beta}(T,\mu) = \frac{1}{e^2T\Omega} \int \sigma_{\alpha\beta}(\varepsilon)(\varepsilon-\mu)^2\left[-\frac{\delta f_0(T,\varepsilon,\mu)}{\delta\varepsilon}\right] d\varepsilon \quad (3)$$

The transport distribution tensor elements in this case are determined by Fourier interpolation of the band structure, denoted by σαβ. The tensor indices are denoted by α and β, while the cell volume, chemical potential, Fermi distribution function, and absolute temperature are represented by Ω, μ, f_0, and T, respectively. The crystal structure and the band structure on a uniform grid are the input data required to execute the BoltzTraP function. The Boltzmann equation [49] is solved by the BoltzTraP algorithm, where f is the distribution function, v is the particle's velocity vector, and k is the wave vector.

$$\frac{\delta}{\delta t}f + \vec{v}\frac{\delta}{\delta\vec{r}}f + \frac{eE}{h}\frac{\delta}{\delta\vec{k}}f = \left(\frac{df}{dt}\right)_{scattering} \quad (4)$$

Several simplifying approximations are introduced: the chemical potential (μ) is set to the Fermi level energy (μF) because conductivities (thermal and electronic) depend proportionally on the relaxation time τ within the constant relaxation time framework; those values can then be simply multiplied by the constant relaxation time (10^{-14} s, as this value is used in BoltzTraP code) to obtain the final transport properties; the Seebeck coefficient does not depend on the relaxation time within the constant relaxation time approximation; the CSTA assumes that the relaxation time τ is independent of energy; as a result, the power factor is τ dependent and ZT is τ independent). The constant relaxation time approximation (CSTA) of $\tau = 10^{-14}$ s is used, to accommodate more electrons scattering and intense lattice vibration within the materials and the temperature increases.

3. Results and Discussions

3.1. Structural Properties

Fig. 1 demonstrates the crystal structures of $MgHfS_3$ and $MgZrS_3$. Our analysis of the output data revealed that the materials contain an orthorhombic perovskite structure. The three-dimensional configuration of the structure and all the necessary properties for the perovskites are shown in Table 1. Regarding experimental and theoretical values for lattice constants, the outcomes agreed with earlier studies. The minimum energy of $MgHfS_3$ is found at 9.59Å and that of MgZrS3 is found at 9. 19Å on a parabolic curve that is produced when the total energy for MgBS3 is plotted against the lattice constants. In terms of optimization, their most optimal point is the one that shows convergence and has the lowest total energy cut-off in relation to the k-point sample curve.

The estimated lattice constants, which are listed in Table 1, correspond well with the experimental data that is currently available. In addition, the formation enthalpy of the compounds is also studied to confirm the materials' capability for synthesis. Balogun et al.'s relation [50] is used to compute low formation enthalpy, which guarantees a compound's ease of synthesis. Our computed values of formation energy closely match the known theoretical results and are presented in Table 1 with the results of the crystal structure analysis.

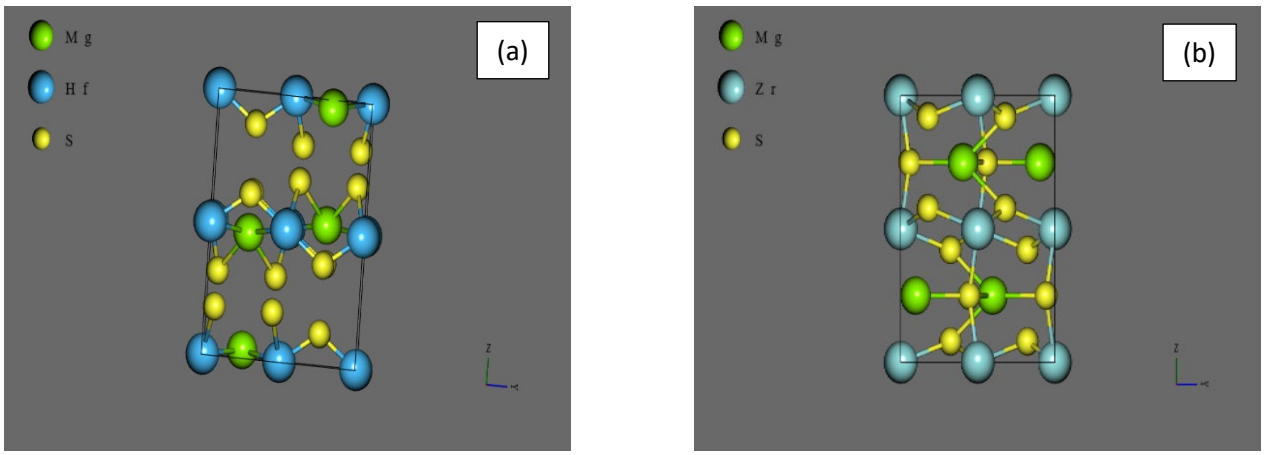

Fig. 1. Crystal Structure of (a) $MgHfS_3$, (b) $MgZrS_3$

Table 1. Calculated GGA lattice constants, bulk modulus B^0, and Moduli derivative B^1

S/N	Crystals	a(Å)	b(Å)	c(Å)	B^0(GPa)	B^1	ΔH_f(eV /atom)
1	**$MgHfS_3$**	6.56	7.02	9.59	78.9	5.57	-1.11
2	$MgZrS_3$	6.56	7.02	9.19	251.3	6.01	-1.05
3	$MgTiS_3$	6.66	7.03	9.27	170.6	4.43	-0.96
4	Expt.	7.56 [52], 8.90 [44]	5.55 [50]. 6.87 [51]				-1.019 [50]
5	BaZrS3-β*	7.02	7.05	9.98	-	-	
6	BaZrS3-α*	7.04	7.15	10.03	-	-	
7	Na6ZnO4	7.55	7.55	5.83	65.25	4.34	-1.16
8	Na_6ZnS4	8.81	8.81	6.94	35.81	4.32	-1.06
9	Na_6ZnSe_4	9.25	9.25	7.12	33.33	4.89	-0.98

*Ref. 56

3.2. Electronic Properties

The quantum-mechanical behaviour of electrons within a material can be explained by the band theory or structure. For the configuration of all atoms, the energy level diagram has bands of levels that match the energy levels in solids in addition to discrete levels. The flow of electrons in the form of currency in a conducting material is made possible by the movement of electrons and holes between the conduction and valance bands, which are situated above the greatest filled level [51]. Nevertheless, because insulators have an energy level that is far higher than the maximum filled level, electrical current cannot pass through them. For classifying materials, the energy gap, a region where there is no electron in the electronic band gap and which corresponds to the bonding and antibonding levels, is significant. The band structure, total density of states (TDOS), and partial density of states (PDOS) of the MgBS3 (B = Hf and Zr) chalcogenide perovskite is shown in Fig. 2. Figures 2a and 2b demonstrate the direct bandgap at the Γ-point of 1.43 eV for MgHfS3 and 1.3 eV for MgZrS3, respectively. Our findings support the notion that alkaline earth chalcogenides are advantageous materials for photovoltaic applications due to their potential for direct band gaps with high optical absorption coefficients that are comparable to those of traditional optoelectronic semiconductors like GaAs and their substantial band dispersion which suggests good carrier mobility. Some chalcogenides in the phase such as $SrZrS_3$, $BaZrSe_3$ and $SrHfSe_3$, display more acceptable band gaps (1.0 eV-1.5 eV) which are identified as the promising materials for solar energy conversion. The electronic structure of $MgZrS_3$ or $MgHfS_3$ was dominated by the chemical bond hybridization of Mg-2p Zr-5d or Hf-5d and S-2p. The binding connection is located inside the atoms closer to the Fermi energy level, as indicated by the density of states (DOS) in Figure 2(a-b). The materials' semiconductor nature is demonstrated by the calculated DOS and PDOS. The materials' conducting nature for solar applications was further confirmed by the bandgap estimate derived from the band structure. The

atomic states of Mg, Hf, Zr, and S were thoroughly examined in the s, p, and d configurations. Hf-5d occupies the valence band region more often than Zr-5d occupies the conduction band region, as seen in Figs. 2(a) and (b). As a result of their higher energy within the region, Zr-5d and Hf-5d occupy distinct conductivity bands. Higher zirconium doping would raise the material's energy level, whereas Hf doping would lower it because fewer electrons are occupied in the conduction band. These boost solar energy's utilization of electron-hole recombination [52]. The obvious overlap between the magnesium and zirconium sulphur equivalents of the DOS structures throughout the energy range indicates that the materials are chemically bound by covalent bonds with minimal ionicity. There are high-symmetry locations in the first Brillouin zone that have been missed in some previous theoretical studies. The bandgap values of magnesium zirconium and hafnium sulphides were determined using the wave-like properties of their band structures [53].

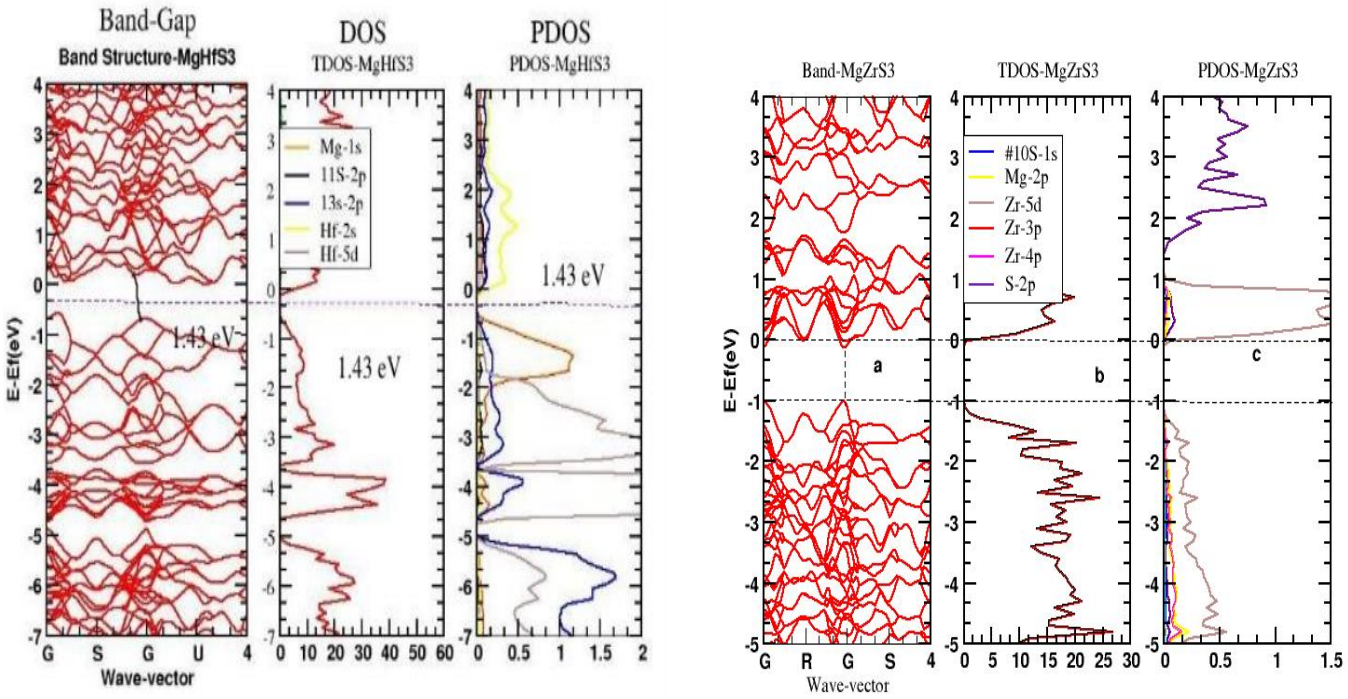

(a) $MgHfS_3$ **(b) $MgZrS_3$**

Fig. 2. Calculated Band Structure, TDOS and PDOS

3.3. Thermoelectric Properties

The figure of merit (zT) is the defining factor for an optimal or perfect thermoelectric material. Fig. 3 represents the figure of merits for MgHfS3 and MgZrS3. The figure of merit for the p region of MgHfS3 increases slightly with temperature, with values of 0.38 at 100K, 0.32 at 200K, 0.35 at 300K, and 0.37 at 500K. In contrast, the figure of merit for MgZrS3 responds differently to temperature increase, with values of 3.5 at 400K, 0.89 at 500K, 0.77 at 600K, and 0.5 at 700K for p regions. This is dependent on the Seebeck coefficient, electrical conductivity, temperature, and thermal conductivity. A greater efficiency in transforming thermal energy into electrical energy is indicated by MgZrS3. This suggests improved functionality and performance for uses such as thermoelectric cooling or waste heat recovery. However, with greater chemical potential at various higher temperatures, MgHfS3 efficiency could be increased. Although their maximum zT is close to ambient temperature and around 600–700 K, respectively, our work is in good agreement with that of the lead chalcogenide PbX (X = S, Se, or Te) and bismuth telluride (Bi2Te3) compounds [54]. However, the toxicity of lead and telluride has recently sparked a lot of interest in research on less dangerous alternatives. In comparison to the binary alloys, the calculated power factor (PF) (shown in Fig. 4) by relaxation time values for $MgHfS_3$ at the p region can reach up to 2.54×10^{11} W/msK^2 at 500K, 1.7×10^{11} W/msK^2 at 400K, 1.32×10^{11} W/msK^2 at 300K, and 8.04×10^{10} W/msK^2 at 200K. In contrast, the PF values for $MgZrS_3$ were found to be 4.54×10^{11} W/msK^2 at 500K, 3.7×10^{11} W/msK^2 at 400K, 2.54×10^{11} W/msK^2 at 300K, and 1.6×10^{11} W/msK^2 at 200K of the order. In addition, the PF value rises as the temperature rises, guaranteeing that the compounds operate at a high temperature. The thermoelectric results indicate that Na_6ZnSe_4 and Na_6ZnS_4 may exhibit superior thermoelectric qualities. Further theoretical and experimental researches on materials for

their use as a new thermoelectric material in medium and high temperatures may be prompted by the surprisingly high PF power factor values for ternary semiconductors [55-57], which suggest an inherent advantage in their electrical and thermal transport properties that was first made known to us here.

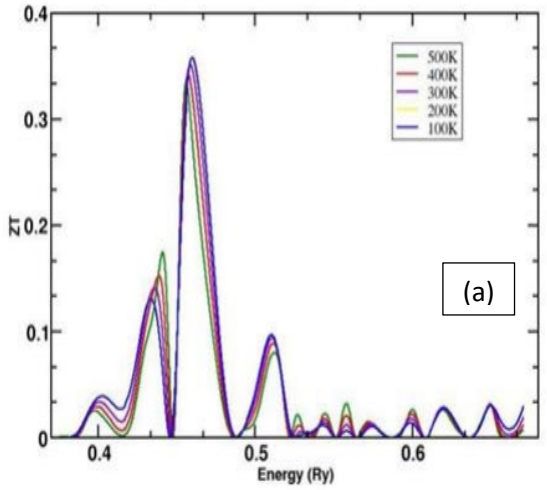

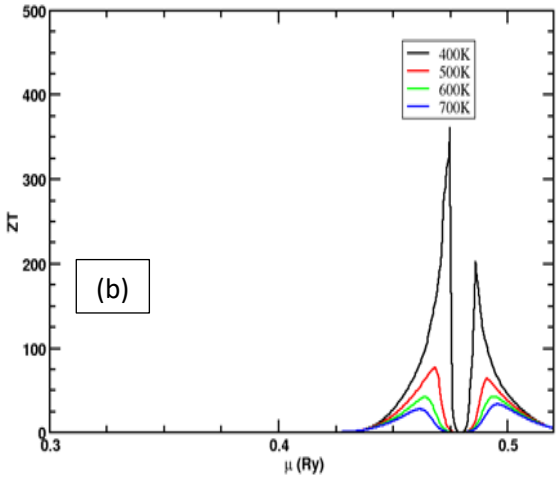

Fig. 3. Figure of Merit for (a) $MgHfS_3$, and (b) $MgZrS_3$

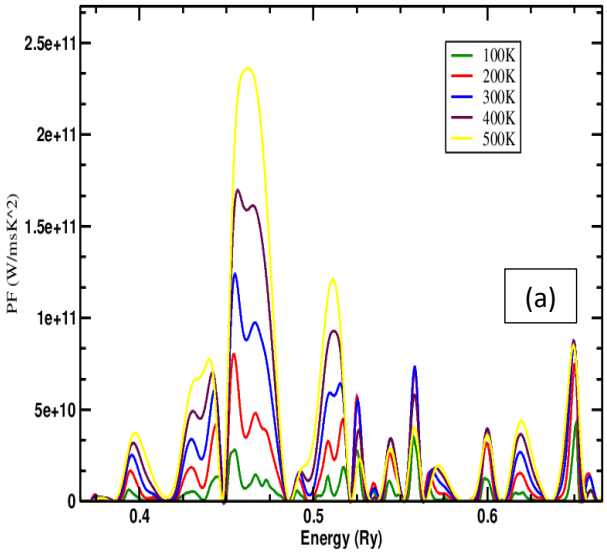

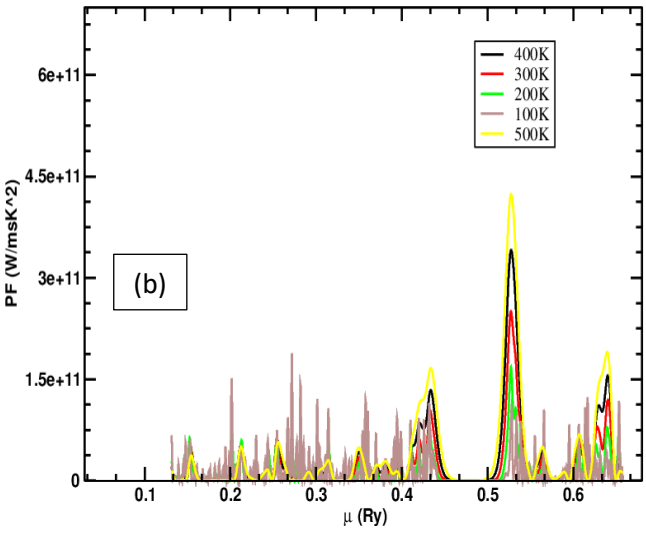

Fig. 4. Power Factor for (a) MgHfS3, and (b) MgZrS3

Only $CuInSe_2$ has an advantage over our materials at 850K, according to a comparison of our PF results with selected chalcogenides materials displaced in Table 2. However, if our materials are subjected to the same temperature as the former, they will fare better than other selected materials in the table. The surprisingly high PF power factor values for ternary semiconductors [57], which were first reported, imply an inherent advantage in their thermal and electrical transport characteristics. This could therefore prompt further theoretical and experimental studies on materials to be used, including new thermoelectric materials at medium and high temperatures. As free electrons migrate from the highest to the lowest temperature, the Seebeck coefficients (S) measure the voltage produced between the two ends of various materials. Fig. 5(a) illustrates how the Seebeck coefficient varies with chemical potential (μ).

Table 2. Carrier concentration, n (e^-/cm^3), the FoM, zT, Power Factor, PF, Seebeck coefficient, S, electrical conductivity σ_{ele}, and thermal conductivity κ_{ele}

#	Crystals	Carrier Con.(e^-cm^3)	zT	PF (W/msK^2)	S(μ V/K)	σ X 10 ^{20} (W/msK)	κ_{ele} X 10 ^{15} (W/ms.K)
1	$MgHfS_3$	10^{19}	0.37 (500K)	2.4 (500K)	650	1.35 (500K)	1.5
2	$MgZrS_3$	10^{19}	0.89 (700K)	4.4 (500K)	2000	1.25 (500K)	0.95
3	Na_6ZnO_4	10^{20}	-	1.4 (800K)			-
4	$CuInSe_2$	10^{21}	0.541 (850K)	4.67 (850K)			7.78
5	Na_6ZnS_4	10^{20}	0.8 (800K)	1.5 (800K)			-
6	$CuBS_2$	10^{20}	0.943 (900K)	1.12 (900K)			1.18, 0.199
7	$NaInSe_2$	10^{18},10^{19}	0.948 (800K)	0.433 (900K)			0.411,0.308

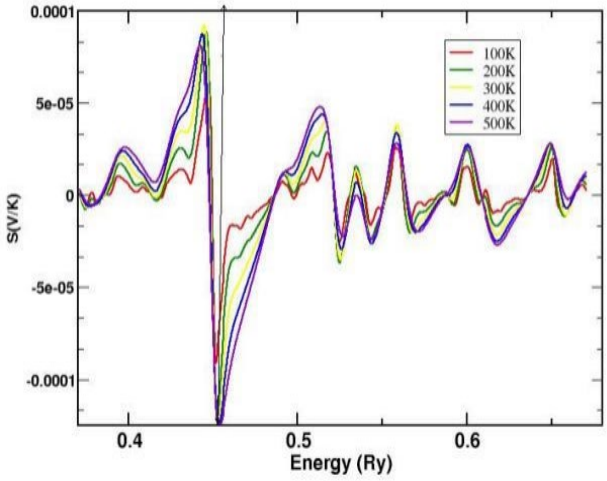

(a) $MgHfS_3$

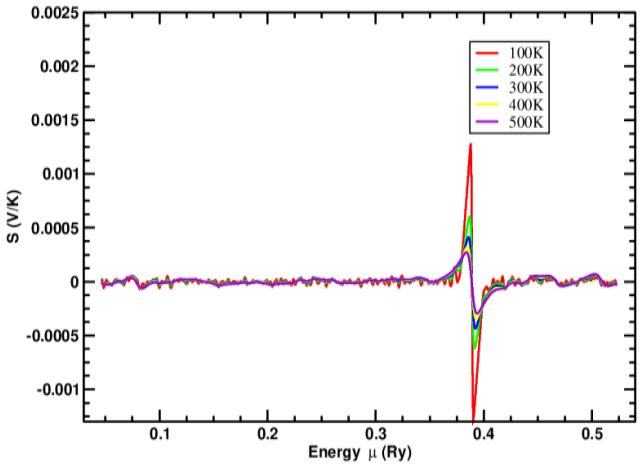

(b) $MgZrS_3$

Fig. 5. Seebeck coefficient

The Seebeck coefficient decreases with increasing temperature, with the corresponding peak values for the p region of $MgHfS_3$ being 2850 μ V/K at 100K, 2100 μ V/K at 200K, 1380 μ V/K at 300K, 1100 μ V/K at 400K, and 650 μ V/K at 500K, and for the n region being − 1200 μ V/K at 100K, − 1050 μ V/K at 200K, − 1350 μ V/K at 300K, − 1280 μ V/K at 400K, and − 1200 μ V/K at 500K . The conduction is area dominant, according to the Seebeck coefficient. When designing thermoelectric devices like energy generators or thermocouples, the material's negative Seebeck coefficient and preponderance of n-type charge carriers are essential. The Seebeck coefficient also decreases in Fig. 5(b) with corresponding values of 2000 μ V/K at 500K, 2500 μ V/K at 400K, 3500 μ V/K at 300K, 780 μ V/K at 200K, and 120 μ V/K at 100K for the p region of $MgZrS_3$, and − 4000 μ V/K at 500K, − 3550 μ V/K at 400K, − 860 μ V/K at 300K, − 300 μ V/K at 200K, and − 400 μ V/K at 100K. These results in a positive Seebeck coefficient, indicating that the material's conduction is dominated by p-type (hole-rich) charge carriers, which are the primary charge carriers for the thermoelectric voltages. Since electrons have enough thermal energy to move from the valence band to the conduction band as the temperature rises, electron-hole pairs are created, and electrical conductivity increases [57-62]. The ability of a substance to carry an electric current is known as electrical conductivity in solids. The presence of free electrons and the band structure of the material are two examples of factors that affect this capacity [63, 64]. As the temperature rises, electrons receive sufficient thermal energy to move from the valence band to the conduction band, producing electron-hole pairs and increasing electrical conductivity. Figure 6 illustrates how electrical conductivity varies with constant relaxation time (σ/τ) as a function of chemical potential μ. This indicates a material's ability to allow electric charges to freely travel and, as a result, how an

electric current flows. To account for increased electron scattering and strong lattice vibration inside the materials as well as temperature increases, the constant relaxation time approximation (CSTA) of $\tau = 10^{-14}$ s is employed.

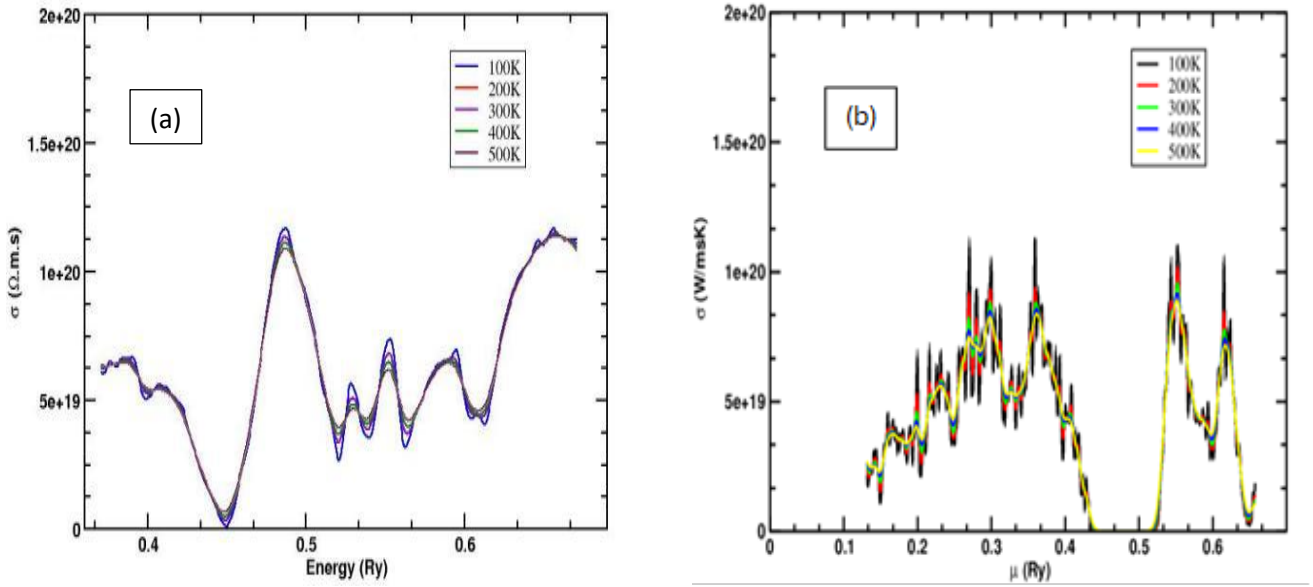

Fig. 6. Electrical conductivity (a) $MgHfS_3$, and (b) $MgZrS_3$

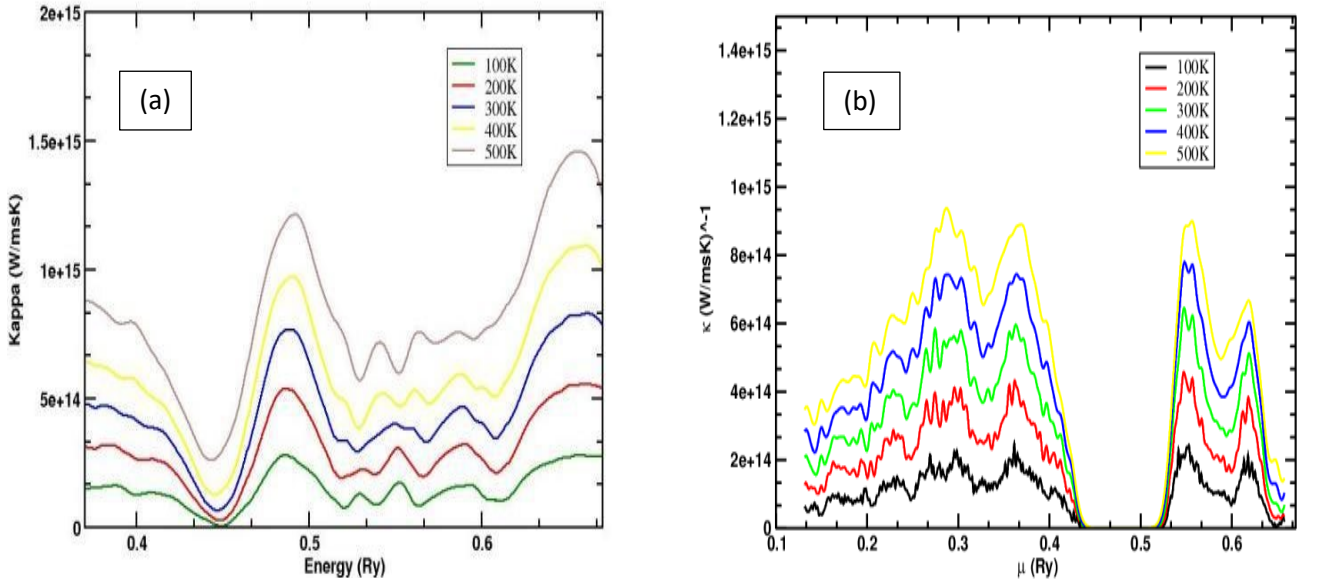

Fig. 7. Thermal conductivity (a) $MgHfS_3$, and (b) $MgZrS_3$

As the temperature rises, the electrical conductivity value decreases slightly. For MgHfS3, the highest peak values are 1.11×10^{20} at 100K, 1.21×10^{20} S/ms at 200K, 1.25×10^{20} S/ms at 300K, 1.30×10^{20} S/ms at 400K, and 1.35×10^{20} S/ms at 500K, as shown in Fig. 6(a). For $MgZrS_3$, peak at 500K is 5.75×10^{19} S/ms and the highest peaks of 1.25×10^{20} S/ms at 400K, 1.05×10^{20} S/ms at 300K, 1.10×10^{20} S/ms at 200K, and 1.00×10^{20} S/ms at 100K are observed, as shown in Fig. 6(b). The observed σ/τ trend is consistent with band theory concepts. It is commonly known that when a semiconductor is heated, charge carriers are formed inside the material. By raising the concentration of carriers, higher temperatures may result in increased electrical conductivity. The greatest value, 1.35×10^{20} S/ms, was observed by $MgHfS_3$ at 500K, but $MgZrS_3$ was claimed to have 1.25×10^{20} S/ms at 400K. Its high σ/τ value strongly suggests that it is a suitable thermoelectric material [65]. Although lattice thermal conductivity is the ability of a solid material to conduct heat through vibrations of its atomic lattice, mainly through the movement of phonons, we neglected the influence of phonons in our simulations because of the ultralow heat

conductivity of the lattice in chalcogenide perovskites [66]. Phonons are quantized vibrations of the lattice that carry thermal energy, and their interaction with other lattice imperfections and each other phonons determine the thermal conductivity. Lattice thermal conductivity (κ_L) measures the efficiency of heat transfer via lattice vibration. To prevent our work from being understudied, we have used every other thermoelectric tool at our disposal to standardize our research and contrast it with the best thermoelectric materials on the market [67]. When creating a suitable thermoelectric material, a substance's capacity to transmit heat from one location to another is crucial. The sum of its electron part (κe) and phonon part (κp) results in the total contribution to the thermal conductivity (κ). Due to the limitations of the BoltzTraP code based on classical theory, only the electronic portion κ has been approximated [68]. Fig. 7 indicates that the materials' thermal conductivity rises with temperature. For $MgHfS_3$, Fig. 7(a) displays peak values of 1.5×10^{15} W/ms at 500K, 1.25×10^{15} W/ms at 400K, 0.89×10^{14} W/ms at 300K, 0.52×10^{14} W/ms at 200K, and 0.25 x 10^{14} W/ms at 100K. For $MgZrS_3$, Fig. 7(b) displays values of 0.95×10^{14} W/ms at 500K, 0.75×10^{14} W/ms at 400K, 0.50×10^{14} W/ms at 300K, 0.4×10^{14} W/ms at 200K, and 0.15×10^{14} W/ms at 100K, all in the positive region of the chemical potential. Our materials' exceptionally low heat conductivity characteristics are a crucial quality for the development of thermoelectric devices. Our data supports the hypothesis that thermal conductivity is frequently significantly stronger at low temperatures than electronic thermal conductivity [69], which is corroborated by additional examination of our results [70]. However, thermal conductivity rapidly decreases at higher temperatures; electronic thermal conductivity predominates in semiconducting materials. As a result, materials such as $MgHfS_3$ and $MgZrS_3$ hold great potential for thermal energy conversion, and researchers ought to be motivated to assess their thermoelectric characteristics for real-world applications. Furthermore, the temperature dependence of electrical conductivity (σ/τ) and electronic thermal conductivity (κe/τ), which both rise with temperature, is shown in Figs. 6 and 7 Both σ/τ and κc/τ rise because of an increase in carrier concentration brought on by temperature changes. Furthermore, $MgBS_3$ is classified as a semiconducting perovskite based on its behaviour. In contrast to ours, the materials in Fig. 5 and Table 2. should only include one type of carrier that shows lower Seebeck coefficient values, 0.0095 for HfS_3 and 0.0015 for ZrS_3, both at 200K, to ensure that the Seebeck coefficient is large. Both charge carriers migrate to the cold end because of mixed n-type and p-type conduction, eliminating the induced Seebeck voltages. Semiconductors and insulators with low carrier concentrations have large Seebeck coefficients; see Equation (3). However, low carrier concentration results in low electrical conductivity. In thermoelectric materials, the figure of merit ZT ($S^2\sigma T/\kappa$), where κ is the thermal conductivity, must be maximized by striking a balance between big S and high electrical conductivity.

Conclusion

The electronic and thermoelectric properties of the two chalcogenide compounds, $MgHfS_3$ and $MgZrS_3$, were investigated using a combination of first-principles band structure calculations with Boltzmann's transport theory under the charge-carrier relaxation time and rigid band approximations. We compared these compounds to other potential TE materials, such as Na_6ZnO_4, $NaInSe_2$, $CuInSe_2$, Na_6ZnS_4, and $CuBS_2$. Our main findings are summarized as follows: The calculated structural parameters and elastic constants agree with the available experimental and theoretical reports. By using the wave-like properties of the band structures of magnesium zirconium and hafnium sulphides to calculate the bandgap values, the improved GGA-PBEsol electronic band structure shows that $MgHfS_3$ is a semiconductor with a direct fundamental band gap Γ-M of a direct bandgap at the Γ-point of 1.43 eV for $MgHfS_3$ and 1.3 eV for $MgZrS_3$. Additionally, the $MgHfS_3$ and $MgZrS_3$ band structures are characterized by a blend of heavy metals such as Hf, Zr, and light charge-carrier effective masses of magnesium and sulfur, which leads to anisotropic and improved TE characteristics.

The p region of the chemical potentials showed that $MgHfS_3$ had a Seebeck coefficient of 650 μ V/K at 500K, whereas the p region showed that $MgZrS_3$ had a significant Seebeck of 200 μ V/K at 500K. The electrical conductivity value falls somewhat as the temperature rises, peaking at 1.35×10^{20} W/msK for $MgHfS_3$ at 500K and 1.25×10^{20} W/msK for $MgZrS_3$ at 400K, with an ideal electro-hole concentration of 1.5×10^{19} cm^{-3}. For p-doped $MgZrS_3$, the optimum figure of merit (zT) is 3.5 at 400K, whereas for p-doped $MgHfS_3$, it was 0.37 at 500K. Although $MgHfS_3$ is not a high-performance material for TE applications as a result, its TE performance can be enhanced by partially substituting heavy elements for its constituent parts.

The primary focus of their zT upgrade is power factor improvement. Developing efficiently doped structures without affecting the crystal structure is a crucial approach for enhancing their power factor. Our materials' low carrier concentration and electrical conductivity are the primary obstacles to reaching high zT. Through appropriate doping, $MgHfS_3$ can achieve higher electrical conductivity and carrier concentration, which can change its electronic structure and lead to a tolerable zT. In contrast to indium and tin chalcogenides, which belong to the mid-temperature range of thermoelectric materials, our findings provide an overview of the current state of knowledge regarding chalcogenides perovskites. The structural characteristics, zT-improvement techniques, thermoelectric characteristics, disadvantages, and uses of materials are all compiled in one comprehensive document. More research is required to enhance the

thermoelectric performance of mid-temperature chalcogenide-based thermoelectric materials, even though a few ideas have been proposed to improve their thermoelectric properties.

Funding Statement

The author declares that there is no known competing financial interests or personal relationships that could have appeared to influence the work reported in this paper.

Conflicts of interest

The authors declare that they have no known competing financial interests or personal relationships that could have appeared to influence the work reported in this paper.

Authors contribution statement

The conceptualization and study design, data collection and computation, data analysis and interpretation, manuscript writing and editing, as well as supervision was done by Rilwan O, Balogun. The final manuscript was edited and proofread by the author.

Availability of data and materials

Datasets and materials will be made available on request

References

[1] Rahman, M.H., Chowdhury, E.H., Redwan, D.A. and Hong, S., 2021. Computational characterization of thermal and mechanical properties of single and bilayer germanene nanoribbon. Computational Materials Science, 190, p.110272.

[2] Kalami, R. and Ketabi, S.A., 2023. Role of Linear Defects on the Electronic, Transport, and Thermoelectric Properties of Armchair Edge Silicene Nanoribbons. *Journal of Electronic Materials,* pp.1-11.

[3] Kalami, R. and Ketabi, S.A., 2023. Electronic and Thermoelectric Properties of Armchair Edge Silicene Nanoribbons: Role of Quantum Antidot Arrays. *Journal of Electronic Materials,* 52(10), pp.6566-6577.

[4] Tsukagoshi, K., Alphenaar, B.W, Ago, H.,1999. Coherent transport of electron spin in a ferromagnetically contacted carbon nanotube, *Nature* 401, 572.

[5] Xiong, Z.H., Wu, D., Vardeny, Z.V., Shi, J., 2004. Giant magnetoresistance in organic spin-valves, *Nature* 427 821.

[6] Dediu, V., Murgia, M., Matacotta, F. C., Taliani, C., Barbanera, S., 2002. Room temperature spin polarized injection in organic semiconductor, *Solid State Commun*. 122 181.

[7] Shim, J.H., Raman, K.V., Park, Y.J., Santos, T.S., Miao, G.X., Satpati, B., Moodera, J.S., 2008. Large spin diffusion length in an amorphous organic semiconductor, *Phys. Rev. Lett*. 100, 226603.

[8] Santos, T.S., Lee, J.S., Migdal, P., Lekshmi, I.C., Satpati, B., Moodera, J.S., 2007. Room temperature tunnel magnetoresistance and spin-polarized tunnelling through an organic semiconductor barrier, *Phys. Rev. Lett*. 98, 016601.

[9] Ouyang, M., Awschalom, D.D., 2003. Coherent spin transfer between molecularly bridged quantum dots, *Science* ,301, 1074.

[10] Petta, J.R., Slater, S.K., Ralph, D.C., 2004. Spin-dependent transport in molecular tunnel junctions, *Phys. Rev. Lett*. 93, 136601.

[11] Sanvito, S., 2007. Memoirs of a spin, *Nature Nanotechnology*, 2, 204.

[12] Ning, Z., Zhu, Y., Wang, J., Guo, H., 2008. Quantitative analysis of nonequilibrium spin injection into molecular tunnel junctions, *Phys. Rev. Lett*.100, 056803.

[13] Bentien, A., Christensen, M., Bryan, J., Sanchez, A., Paschen, S., Steglich, F., Stucky, G.D., and Iversen, B.B. 2004., *Phys. B*, 69, 045107 (2004).

[14] Shokri, A. and Salami, N., 2019. Thermoelectric properties in monolayer MoS2 nanoribbons with Rashba spin–orbit interaction. *Journal of Materials Science*, 54(1), pp.467-482.

[15] Checkelsky, J.G. and Ong, N.P., 2009. Thermopower and Nernst effect in graphene in a magnetic field. *Physical Review B*, 80(8), p.081413.

[16] Yan, Y., Liang, Q.F., Zhao, H., Wu, C.Q. and Li, B., 2012. Thermoelectric properties of one-dimensional graphene antidot arrays. *Physics Letters A*, 376(35), pp.2425-2429.

[17] Domínguez-Adame, F., Martín-González, M., Sánchez, D. and Cantarero, A., 2019. Nanowires: A route to efficient thermoelectric devices. *Physica E: Low-dimensional Systems and Nanostructures*, 113, pp.213-225.

[18] Kalami, R., & Ketabi, S. A. 2021. Spin-dependent thermoelectric properties of a magnetized zigzag graphene nanoribbon. *Progress in Physics of Applied Materials*, 1(1), 1-6.

[19] Kalami, R., & Ketabi, S. A. 2023. Comparison of thermoelectric properties of armchair germanene nanoribbon and armchair germanene nanomesh. *Progress in Physics of Applied Materials,*3(2),169-176.

[20] Zhang, K. B., Tan, S. H., Peng, X. F., & Long, M. Q. 2024. Electronic and thermoelectric properties in SnS-nanoribbon-based heterojunctions. *Chinese Physics Letters*, 41(9), 097301.

[21] Song, T. T., Yang, N. X., Wang, R., Liao, H., Song, C. Y., & Cheng, X. Y. 2024. Enhanced thermoelectric performance of graphene p–n junction nanoribbon. *Physica E: Low-dimensional Systems and Nanostructures*, 164, 116057.

[22] Nolas, G.S., Cohn, J.L., Slack, G.A., and Schujman, S.B., 1998. *Appl. Phys. Lett*. 73, 178.

[23] May, A.F., Toberer, E.S., Saramat, A and Snyder, G.J., 2009. *Phys. Rev. B*, 80, 125205.

[24] Christensen, M., Lock, N., Overgaard, J., and Iversen, B.B., 2006. *J. Am. Chem. Soc*. 128, 15657.

[25] Sales, B.C., Mandrus, D., and Williams, R.K., 1996. *Science*, 272, 1325.

[26] Rull-Bravo, M.; Moure, A.; Fernández, J.; Martín-González, M. Skutterudites as thermoelectric materials: 2015. Revisited. *RSC Adv*. 5, 41653–41667.

[27] Tan, G.; Zhao, L.-D.; Kanatzidis, M.G. Rationally designing high-performance bulk thermoelectric materials. Chem. Rev. 2016, 116, 12123–12149.

[28] Pichanusakorn, P.; Kuang, Y.; Patel, C.; Tu, C.; Bandaru, P. 2012. Feasibility of enhancing the thermoelectric power factor in GaNx As1−x. *Phys. Rev. B*, 86, 085314.

[29] Ouardi, S.; Fecher, G.H.; Felser, C.; Schwall, M.; Naghavi, S.S.; Gloskovskii, A.; Balke, B.; Hamrle, J.; Postava, K.; Pištora, J. 2012. Electronic structure and optical, mechanical, and transport properties of the pure, electron-doped, and hole-doped Heusler compound CoTiSb. Phys. Rev. B, 86, 045116.

[30] Kim, H.; Kaviany, M. 2012. Effect of thermal disorder on high figure of merit in PbTe. *Phys. Rev. B*, 86, 045213.

[31] Kerdsongpanya, S.; Alling, B.; Eklund, P. 2012. Effect of point defects on the electronic density of states of ScN studied by first-principles calculations and implications for thermoelectric properties. *Phys. Rev. B*, 86, 195140.

[32] Hoat, D. 2022. Comparative study of structural, electronic, optical and thermoelectric properties of GaS bulk and monolayer. *Philos. Mag*. 99, 736–751.

[33] Hoat, D.; Naseri, M.; Ponce-Perez, R.; Hieu, N.N.; Vu, T.V.; Rivas-Silva, J.; Cocoletzi, G.H. 2020. Reducing the electronic band gap of BN monolayer by coexistence of P (As)-doping and external electric field. *Superlattices Microstruct.* 137, 106357.

[34] Naseri, M.; Hoat, D.2019. Prediction of 2D Li2X (X = Se, Te) monolayer semiconductors by first principles calculations. *Phys. Lett. A*, 383, 125992.

[35] Hong, M.; Wang, Y.; Liu, W.; Matsumura, S.; Wang, H.; Zou, J.; Chen, Z.G. Arrays of planar vacancies in superior thermoelectric Ge1−x−yCdxBiyTe with band convergence. Adv. Energy Mater. 2018, 8, 1801837.

[36] Tang, G.; Liu, J.; Zhang, J.; Li, D.; Rara, K.H.; Xu, R.; Lu, W.; Liu, J.; Zhang, Y.; Feng, Z. 2018. Realizing high thermoelectric performance below phase transition temperature in polycrystalline snse via lattice anharmonicity strengthening and strain engineering. *ACS Appl. Mater. Interfaces*, 10, 30558–30565.

[37] Gayner, C.; Kar, K.K. 2016. Recent advances in thermoelectric materials. *Prog. Mater. Sci.* 83, 330–382.

[38] Ju, H.; Kim, M.; Kim, J. 2015. A facile fabrication of n-type Bi2Te3 nanowire/graphene layer by-layer hybrid structure and their improved thermoelectric performance. *Chem. Eng. J.*, 102–112.

[39] Han, C.; Sun, Q.; Li, Z.; Dou, S.X. 2016. Thermoelectric enhancement of different kinds of metal chalcogenides. *Adv. Energy Mater*. 6, 1600498.

[40] Jeffery L. Gray, 2011. The physics of the solar cell, *Handbook of photovoltaic science and engineering* 2, 82–128.

[41] Mukesh Jain, edition, II-VI Semiconductor Compounds, World scientific, 1993.

[42] Liu, M.L.; Chen, I.W.; Huang, F.Q.; Chen, L.D. Improved thermoelectric properties of Cu-doped quaternary chalcogenides of Cu2CdSnSe4. Adv. Mater. **2009**, 21, 3808–3812.

[43] Sevik, C.; Çagın, T. 2010. Abinitio study of thermoelectric transport properties of pure and doped quaternary compounds. *Phys. Rev. B*, 82, 045202.

[44] Ibáñez, M.; Zamani, R.; LaLonde, A.; Cadavid, D.; Li, W.; Shavel, A.; Arbiol, J.; Morante, J.R.; Gorsse, S.; Snyder, G.J. 2012. Cu2ZnGeSe4 nanocrystals: Synthesis and thermoelectric properties. *J. Am. Chem. Soc*, 134, 4060–4063.

[45] Zeier, W.G.; Heinrich, C.P.; Day, T.; Panithipongwut, C.; Kieslich, G.; Brunklaus, G.; Snyder, G.J.; Tremel, W. 2014. Bond strength dependent superionic phase transformation in the solid solution series Cu2ZnGeSe4−xSx. *J. Mater. Chem. A*, 2, 1790–1794.

[46] Navrátil, J.; Kucek, V.; Plecháček, T.; Cernošková, E.; Laufek, F.; Drašar, C.; Knotek, P. 2014. Thermoelectric Properties of Cu2HgSnSe4 -Cu2HgSnTe4 Solid Solution. *J. Electron. Mater.*43, 3719–3725.

[47] Bekki, B.; Amara, K.; Marbouh, N.; Khelfaoui, F.; Benallou, Y.; Elkeurti, M.; Bentayeb, A. Theoretical study of structural, elastic and thermodynamic properties of Cu2MgSnX4 (X = S, Se and Te) quaternary compounds. *Comput. Condens. Matter* 2019, 18, e00339.

[48] Guin, S.N.; Chatterjee, A.; Biswas, K. Enhanced thermoelectric performance in p-type AgSbSe2 by Cd-doping. RSC Adv. 2014, 4, 11811–11815.

[49] Li, D.; Qin, X.; Zou, T.; Zhang, J.; Ren, B.; Song, C.; Liu, Y.; Wang, L.; Xin, H.; Li, J. 2015. High thermoelectric properties for Sn-doped AgSbSe2. *J. Alloys Compd.* 635, 87–91.

[50] Balogun, R.O., Olopade, M.A., Oyebola, O.O., Adewoyin, A.D., 2021. First-principle calculations to investigate structural, electronic and optical properties of MgHfS3,*Materials Science and Engineering: B*, Volume 273,115405, ISSN 0921-5107,

[51] Oyebola Olusola Olurotimi, Belewu Fatai Damilola, Balogun Rilwan Oluwanishola, Adegboyega Anthony Babajide and Oyebode Daniel Oluwatimilehin, 2024. Exploring the Thermoelectric Potential of Trigonal MgS_2: A Computational Investigation Using DFT and Boltzmann Transport Theory. *Communication in Physical Sciences,*11(2): 288-298

[52] Adegboyega, A.B, Olopade, M.A., Ogungbemi, K.I., Balogun, R.O., 2024. Electro-optical and thermoelectric properties of perovskite CsKAgBiX6(X=Cl,Br,I): A DFT study, *Computational Condensed Matter*,Volume 38,e00878,ISSN 2352-2143, https://doi.org/10.1016/j.cocom.2023.e00878.

[53] Lee, J.K.; Oh, M.-W.; Ryu, B.; Lee, J.E.; Kim, B.-S.; Min, B.-K.; Joo, S.-J.; Lee, H.-W.; Park, S.-D. 2017. Enhanced thermoelectric properties of AgSbTe2 obtained by controlling heterophases with Ce doping. *Sci. Rep.*7, 4496.

[54] Ching, W.-Y.; Rulis, P. Electronic Structure Methods for Complex Materials: The Orthogonalized Linear Combination of Atomic Orbitals; Oxford University Press: Oxford, UK, 2012.

[55] Giannozzi, P.; Baroni, S.; Bonini, N.; Calandra, M.; Car, R.; Cavazzoni, C.; Ceresoli, D.; Chiarotti, G.L.; Cococcioni, M.; Dabo, I. 2009. QUANTUM ESPRESSO: A modular and open-source software project for quantum simulations of materials. *J. Phys. Condens. Matter*, 21, 395502.

[56] Hasan, S.; Adhikari, P.; Baral, K.; Ching, W.-Y. 2020. Conspicuous interatomic bonding in chalcogenide crystals and implications on electronic, optical, and elastic properties. AIP Adv,10, 075216.

[57] Hasan, S.; Baral, K.; Li, N.; Ching, W.-Y. 2021. Structural and physical properties of 99 complex bulk chalcogenides crystals using first-principles calculations. *Sci. Rep*, 11, 9921.

[58] Kresse, G.; Furthmüller, J. 1996. Efficient iterative schemes for ab initio total-energy calculations using a plane-wave basis set. *Phys. Rev. B*, 54, 11169.

[59] Dharmawardhana, C.; Bakare, M.; Misra, A.; Ching, W.Y. 2016. Nature of interatomic bonding in controlling the

mechanical properties of calcium silicate hydrates. *J. Am. Ceram. Soc*. 99, 2120–2130.

[60] Adhikari, P.; Khaoulaf, R.; Ez-Zahraouy, H.; Ching, W.-Y. 2017. Complex interplay of interatomic bonding in a multi-component pyrophosphate crystal: K2Mg (H2P2O7)2 H2O. *R. Soc. Open Sci.* 4, 170982.

[61] Poudel, L.; Tamerler, C.; Misra, A.; Ching, W.-Y. 2017. Atomic-Scale Quantification of Interfacial Binding between Peptides and Inorganic Crystals: The Case of Calcium Carbonate Binding Peptide on Aragonite. *J. Phys. Chem. C*,121, 28354–28363. [

[62] San, S.; Li, N.; Tao, Y.; Zhang, W.; Ching, W.Y. 2018. Understanding the atomic and electronic origin of mechanical property in thaumasite and ettringite mineral crystals. *J. Am. Ceram. Soc*, 101, 5177–5187.

[63] Hunca, B.; Dharmawardhana, C.; Sakidja, R.; Ching, W.-Y. Ab initio calculations of thermomechanical properties and electronic structure of vitreloy Zr41.2Ti13.8Cu12.5Ni10Be22.5. Phys. Rev. B 2016, 94, 144207.

[64] Ching, W.Y.; Yoshiya, M.; Adhikari, P.; Rulis, P.; Ikuhara, Y.; Tanaka, I. First-principles study in an inter-granular glassy film model of silicon nitride. J. Am. Ceram. Soc. 2018, 101, 2673–2688.

[65] Balogun, Rilwan Oluwanishola., Olopade, Muteeu O, Oyebola, Olusola O and Adewoyin, Adeyinka D., 2024. In-silico investigation of photovoltaic performance of $MgXS_3$ (X= Ti and Zr) chalcogenide perovskites compounds. *Archives of Metallurgy and Materials*. Arch. Metall. Mater. 69, 3, 943-954

[66] Ching, W.-Y.; Poudel, L.; San, S.; Baral, K. 2019.Interfacial interaction between suolunite crystal and silica binding peptide for novel bioinspired cement. *ACS Comb. Sci*. 21, 794– 804.

[67] Poudel, L.; Twarock, R.; Steinmetz, N.F.; Podgornik, R.; Ching, W.-Y. 2017. Impact of Hydrogen Bonding in the Binding Site between Capsid Protein and MS2 Bacteriophage ssRNA. *J. Phys. Chem. B*, 121, 6321–6330.

[68] Adhikari, P.; Li, N.; Shin, M.; Steinmetz, N.F.; Twarock, R.; Podgornik, R.; Ching, W.- Y. 2020. Intra-and intermolecular atomic-scale interactions in the receptor binding domain of SARS-CoV-2 spike protein: Implication for ACE2 receptor binding. *Phys. Chem. Chem. Phys*. 22, 18272–18283.

[69] Mulliken, R.S. 1955. Electronic population analysis on LCAO–MO molecular wave functions. I. *J. Chem. Phys*., 23, 1833–1840.

[70] Dharmawardhana, C.; Misra, A.; Ching, W.-Y. Quantum mechanical metric for internal cohesion in cement crystals. Sci. Rep. 2014, 4, 7332.